Available online at www.sciencedirect.com
ScienceDirect
Engineering Fracture Mechanics 75 (2008) 694–704
Engineering Fracture Mechanics
www.elsevier.com/locate/engfracmech

Fatigue crack propagation damaging micromechanisms in ductile cast irons

M. Cavallini [a], O. Di Bartolomeo [b], F. Iacoviello [b,*]

[a] *Università di Roma La Sapienza, I.C.M.M.P.M., via Eudossiana 18, Roma, Italy*
[b] *Università di Cassino, Di.M.S.A.T., via G. Di Biasio 43, 3043 Cassino (FR), Italy*

Received 31 October 2006; received in revised form 28 January 2007; accepted 3 February 2007
Available online 13 February 2007

Abstract

Ductile iron discovery in 1948 gave a new lease on life to the cast iron family. In fact, these cast irons are characterized both by a high castability and by high toughness values, combining cast irons and steel good properties. Ductile cast irons are also characterized by high fatigue crack propagation resistance, although this property is still not widely investigated.

In the present work, three different ferritic–pearlitic ductile cast irons, characterized by different ferrite/pearlite volume fractions, and an austempered ductile cast iron were considered. Their fatigue crack propagation resistance was investigated in air by means of fatigue crack propagation tests according to ASTM E647 standard, considering three different stress ratios ($R = K_{min}/K_{max} = 0.1; 0.5; 0.75$). Crack paths were investigated by means of a crack path profile analysis performed with an optical microscope. Crack surfaces were extensively analysed by means of a scanning electron microscope both considering a traditional procedure and performing a quantitative analysis of 3D reconstructed surfaces, mainly focusing graphite nodules debonding.

Keywords: Ductile cast iron; Fatigue crack growth

1. Introduction

In the first half of the last century, the goal of a combination of good castability and high toughness values was partially fulfilled by malleable iron by means of an extended annealing treatment of white iron. During this heat treatment, cementite decomposes to graphite that precipitates as aggregates in a matrix whose microstructure (ferrite or pearlite) depends on the cooling cycle from the annealing temperature. High costs related to the extended annealing treatment and the difficulty to cast sound white iron components limited its utilization. In 1943, in the International Nickel Company Research Laboratory, a magnesium addition allowed to obtain a cast iron containing not flakes but nearly perfect graphite spheres. In 1948, a small amount of cerium allowed to obtain the same result. Ductile cast irons are now widely used in a number of applications,

* Corresponding author. Tel./fax: +39 0 7762993681.
E-mail address: iacoviello@unicas.it (F. Iacoviello).

0013-7944/$ - see front matter © 2007 Elsevier Ltd. All rights reserved.
doi:10.1016/j.engfracmech.2007.02.002

e.g. wheels, gears and crankshafts in cars and trucks. These cast irons are characterized by a very good combination of overall properties: high ductility (up to more than 18%), high strength (up to 850 MPa and, considering austempered ductile iron, up to 1600 MPa) and good wear resistance. Matrix controls these good mechanical properties and matrix names are used to designate spheroidal cast iron types. Ferritic ductile irons are characterized by good ductility and a tensile strength that is equivalent to a low carbon steel. Pearlitic ductile irons shows high strength, good wear resistance and moderate ductility. Ferritic–pearlitic grades properties are intermediate between ferritic and pearlitic ones. Martensitic ductile irons show very high strength, but low levels of toughness and ductility. Bainitic grades are characterized by a high hardness. Austenitic ductile irons show good corrosion resistance, good strength and dimensional stability at high temperature. Austempered grades show a very high wear resistance and fatigue strength [1,2].

In this work, four different ductile irons were considered: three ferritic–pearlitic and an austempered ductile irons. Their fatigue crack propagation resistance was investigated considering the influence of loading conditions (three different load ratios). Fracture surface was investigated by means of light optical microscope crack profile analysis and by means of SEM fracture surface analysis. Furthermore, a quantitative analysis of 3D reconstructed surfaces was performed, mainly focusing the graphite nodules debonding mechanisms.

2. Materials and experimental methods

Four ductile irons with different microstructures were considered, and chemical compositions are shown in Tables 1–4.

Investigated ferritic–pearlitic ductile irons are characterized by a very high graphite elements nodularity (Fig. 1). This implies that graphite elements could be considered as perfect spheres embedded in a metal matrix.

After the austempering treatment, austempered ductile iron is characterized by a reduced graphite spheroids degeneration and a good homogeneity of bainitic microstructure is obtained, with some residual ferrite around graphite elements (Fig. 2). In this case, graphite elements could be only roughly approximated to spheres.

Table 1
Ductile iron EN GJS350-22 chemical composition (100% ferrite)

C	Si	Mn	S	P	Cu	Cr	Mg	Sn
3.66	2.72	0.18	0.013	0.021	0.022	0.028	0.043	0.010

Table 2
Ductile iron EN GJS500-7 chemical composition (50% ferrite–50% pearlite)

C	Si	Mn	S	P	Cu	Cr	Mg	Sn
3.65	2.72	0.18	0.010	0.03	–	0.05	0.055	0.035

Table 3
Ductile iron EN GJS700-2 chemical composition (5% ferrite–95% pearlite)

C	Si	Mn	S	P	Cu	Mo	Ni	Cr	Mg	Sn
3.59	2.65	0.19	0.012	0.028	0.04	0.004	0.029	0.061	0.060	0.098

Table 4
Austempered ductile iron GGG 70BA chemical composition (fully bainitic)

C	Si	Mn	Mo	Ni	Sn	S
3.61	2.23	0.32	0.42	0.52	0.045	0.015

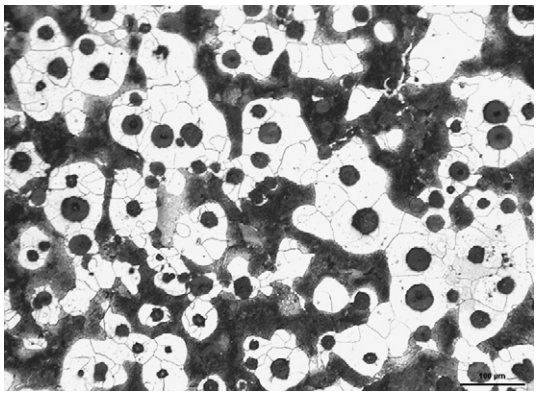

Fig. 1. Ferritic–pearlitic ductile iron microstructure (Nital 3).

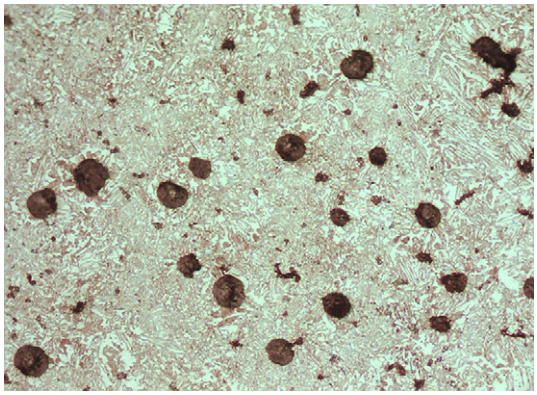

Fig. 2. Austempered ductile iron (ADI) microstructure (Nital 3).

Fatigue crack propagation tests were run according to ASTM E647 standard [3], using 10 mm thick CT (Compact Type) specimens and considering three different stress ratio values (e.g. $R = P_{min}/P_{max} = 0.1$; 0.5; 0.75). Tests were performed using a computer controlled INSTRON 8501 servohydraulic machine in constant load amplitude conditions, considering a 20 Hz loading frequency, a sinusoidal loading waveform and laboratory conditions. Crack length measurements were performed by means of a compliance method using a double cantilever mouth gauge and controlled using an optical microscope (40×).

Crack paths analysis was performed by means of a light optical microscope (LOM), according to the following procedure:

- Fracture surface nickel coating (in order to protect fracture surface during cutting).
- Fractured specimen longitudinal cutting, at half thick, along the fatigue crack propagation direction (by means of a diamond saw).
- Metallographic preparation of the section (up to 0.2 μm Al_2O_3 powder).
- Nital 4 chemical etching (5 s).

Fracture surfaces were analysed by means of a Philips scanning electron microscope (SEM). A 3D fracture surface reconstruction procedure was performed, in order to obtain a quantitatively reconstructed fracture surface and to obtain a quantitative analysis of the microstructure influence on the graphite elements debonding morphology [4]. Corresponding to the same specimen position, a stereoscopic image was obtained performing an eucentric tilting around the vertical axis and capturing two different images, with a tilting angle equal to 5°. A 3D surface reconstruction was performed by means of Alicona MeX software, obtaining images as in Fig. 3. Fracture surface profiles were quantitatively investigated as reported in Fig. 4.

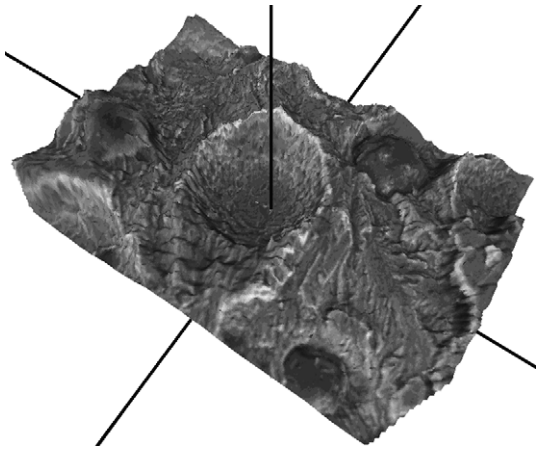

Fig. 3. 3D reconstructed fracture surface (50% ferrite–50% pearlite).

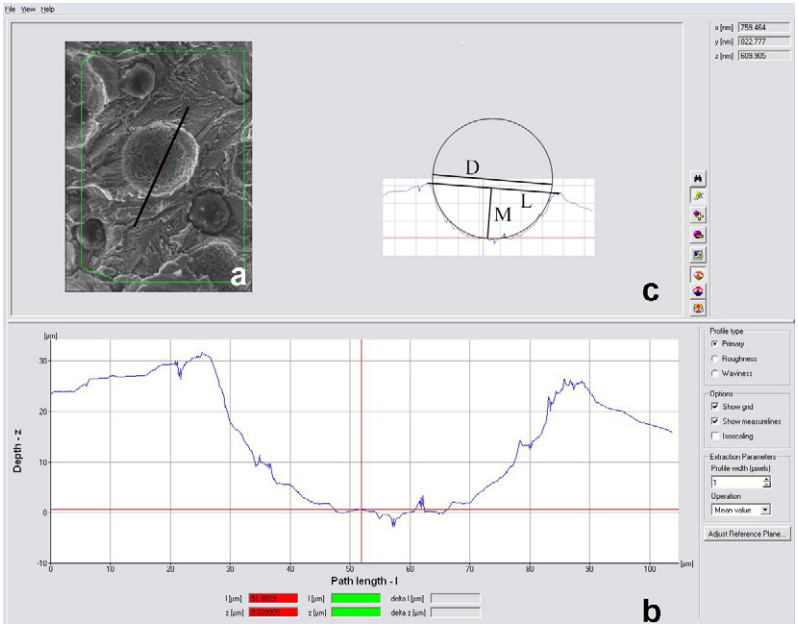

Fig. 4. Fracture surface profile quantitative analysis.

At least 50 voids were considered for all the considered ductile irons and fracture surface profiles were quantitatively investigated as reported in Fig. 4.

Each void was characterized considering an approximation sphere and its geometry, and three different geometrical parameters were considered:

– Void depth "M" (μm).
– Void diameter "L" (μm).
– Approximation sphere diameter "D" (μm).

Relations among these geometric parameters depend on debonding process. If graphite elements debonding is completely fragile, it follows that $M \leqslant D/2$ and $L \leqslant D/2$. On the other side, a ductile debonding process implies $M > D/2$ and $L > D/2$, with differences that increase with the importance of ductile damage mechanism.

3. Results

Stress ratio and microstructure influence on fatigue crack propagation are shown in Fig. 5. For $R = 0.1$, the microstructure influence is almost negligible. The increase of the stress ratio implies an increase of the microstructure influence, with the ferritic–pearlitic (50–50%) and the austempered ductile iron that are characterized by lower crack growth rates for the same applied ΔK values, in stages II and III (Paris stage and final rupture stage), and higher final rupture values. Lower ΔK values are not clearly influenced by microstructure, and they decrease with the increase of the stress ratio for the same crack growth rate.

SEM fracture surface ''traditional'' analysis (Figs. 6, 8, 10, 12 and 14) and crack profile LOM analysis (Figs. 7, 9, 11, 13 and 15) show microstructure influence on fatigue crack propagation micromechanisms (crack growths from left to right) [5–7].

Fatigue crack propagation micromechanisms in ferritic ductile iron are connected both to the ductile striation generation and to an evident cleavage (Fig. 6), for all the loading condition (not depending on R or ΔK). Furthermore, a graphite spheroids debonding is shown both for lower and for higher ΔK and R values (Fig. 7). This debonding does not imply automatically a complete spheroid loosing from the surface. Also spheroids that have less that half of their surface in contact with ferritic matrix do not loose their grip to the surface. As a consequence, closure effect is enhanced by graphite spheroids presence. If the spheroid looses completely the grip with the ferritic matrix, the matrix ductile deformation implies an increase of the hole dimension with a mechanism that is similar to the microvoid growth in dimples formation. If the debonding is not complete, also the void growth is not complete, but however evident (Fig. 7).

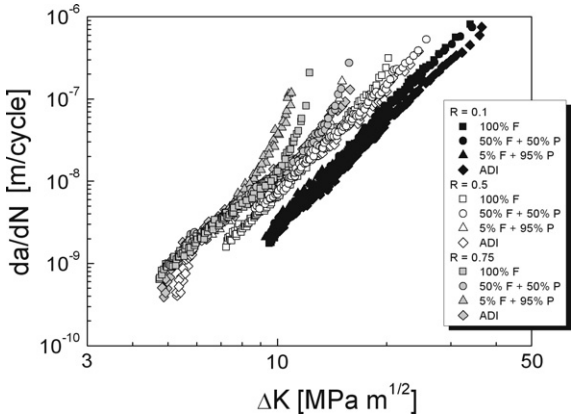

Fig. 5. Microstructure and stress ratio influence on fatigue crack propagation.

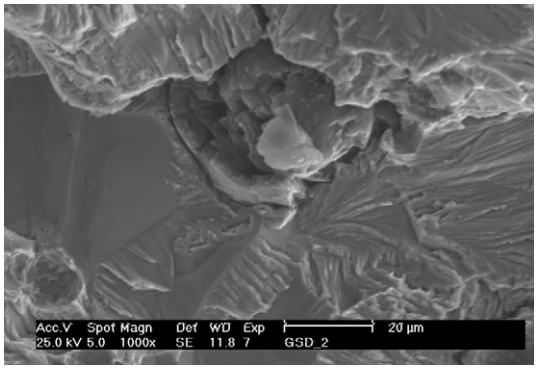

Fig. 6. SEM fracture surface analysis: ferritic ductile iron ($R = 0.5$, $\Delta K = 10$ MPa $\sqrt{\text{m}}$).

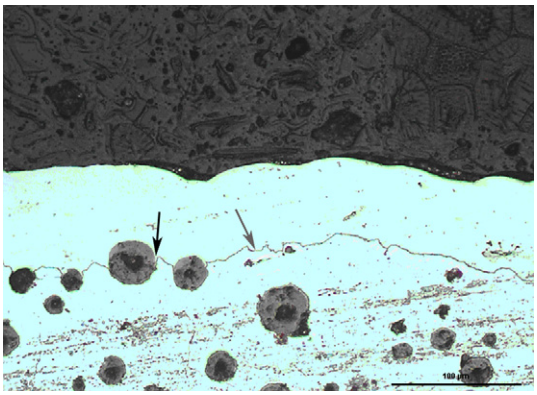

Fig. 7. LOM crack path analysis: ferritic ductile iron ($R = 0.5$, $\Delta K = 10$ MPa $\sqrt{\text{m}}$).

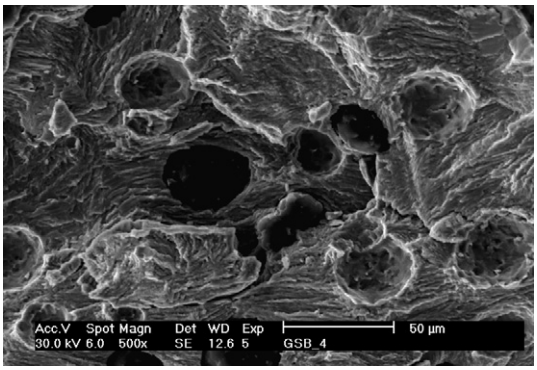

Fig. 8. SEM fracture surface analysis: pearlitic ductile iron ($R = 0.5$, $\Delta K = 10$ MPa $\sqrt{\text{m}}$).

Pearlitic ductile iron shows a different fracture surface morphology, that always does not depend on ΔK or R values. Secondary cracks and both ductile and fragile striations are the main fatigue crack propagation micromechanisms (Fig. 8). Graphite spheroids debonding is often complete, and a reduced void growth is observed (Fig. 9). Spheroid gripping on fracture surface is possible only if at least half of the spheroid surface is in contact with the pearlitic matrix, but this condition is not sufficient. After this spheroid fragile debonding, it is possible to observe that the surface inside the hole shows an evident microductility, consisting in micro-dimples generation.

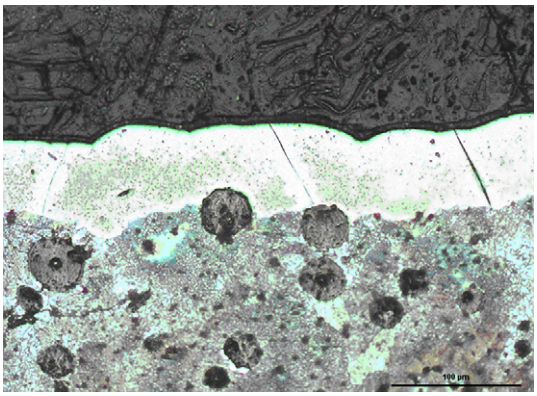

Fig. 9. LOM crack path analysis: pearlitic ductile iron ($R = 0.5$, $\Delta K = 10$ MPa $\sqrt{\text{m}}$).

Ferritic–pearlitic ductile iron shows fatigue crack propagation micromechanisms that are influenced by its microstructure. Ferritic shields are often fractured by cleavage and pearlitic matrix shows the same fracture morphology of the fully pearlitic ductile iron. No evidence of secondary cracks is observed (Fig. 10). Graphite spheroids debonding depends on the loading conditions and is evidently influenced by the metal matrix. Considering lower ΔK values, fracture profile does not show voids growth (Fig. 11) as in pearlitic ductile iron. Considering higher applied ΔK values, ferritic shields are more and more stressed and a ductile debonding becomes more and more evident (Figs. 12 and 13). As a consequence of this ductile debonding, graphite spheroids act as crack closure effect raisers, as in ferritic ductile iron.

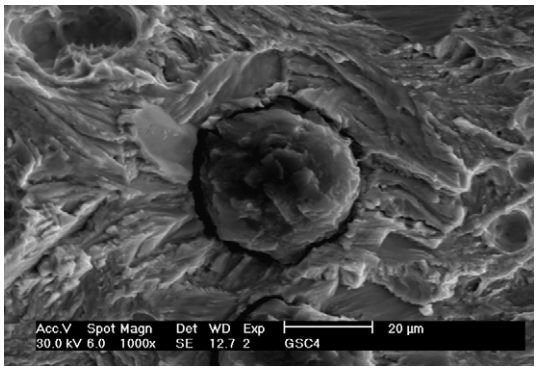

Fig. 10. SEM fracture surface analysis: ferritic–pearlitic ductile iron ($R = 0.5$, $\Delta K = 10$ MPa $\sqrt{\text{m}}$).

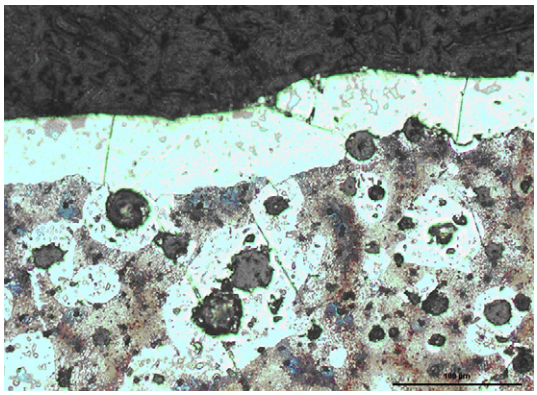

Fig. 11. LOM crack path analysis: ferritic–pearlitic ductile iron ($R = 0.5$, $\Delta K = 10$ MPa $\sqrt{\text{m}}$).

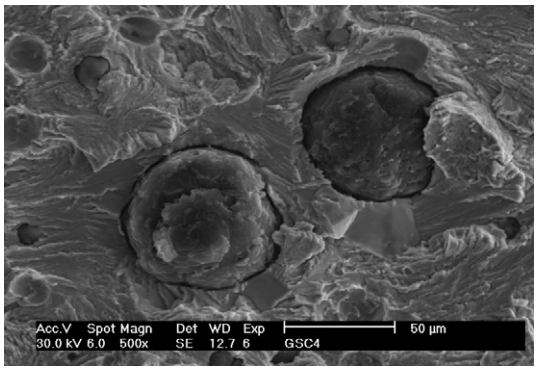

Fig. 12. SEM fracture surface analysis: ferritic–pearlitic ductile iron ($R = 0.5$, $\Delta K = 20$ MPa $\sqrt{\text{m}}$).

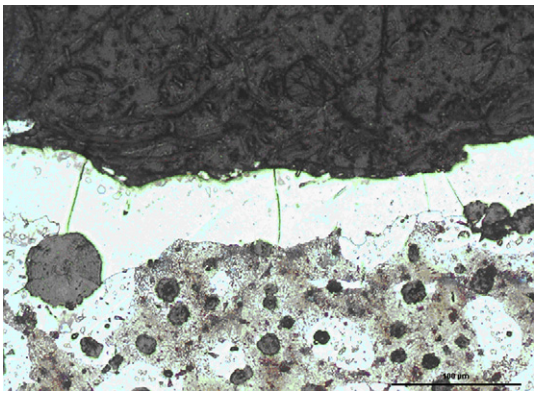

Fig. 13. LOM crack path analysis: ferritic–pearlitic ductile iron ($R = 0.5$, $\Delta K = 20$ MPa $\sqrt{\text{m}}$).

Austempered ductile iron fracture surface is characterized by the presence of striations and cleavage for all the investigated loading conditions, with a graphite elements debonding that is similar to ferritic and ferritic–pearlitic ductile irons and some secondary cracks (Fig. 14). Corresponding to some partially degenerated graphite elements, debonding is not evident. The presence of residual ferrite implies a graphite elements debonding mechanism that is similar to ferritic–pearlitic ductile iron, and also in this case graphite spheroids act as crack closure effect raisers (Fig. 15).

Fig. 14. SEM fracture surface analysis: austempered ductile iron ($R = 0.5$, $\Delta K = 10$ MPa $\sqrt{\text{m}}$).

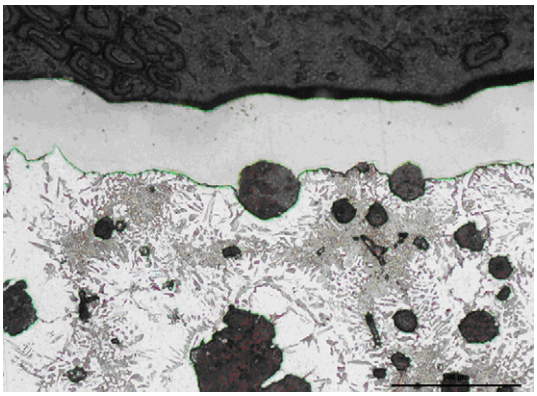

Fig. 15. LOM crack path analysis: austempered ductile iron ($R = 0.5$, $\Delta K = 10$ MPa $\sqrt{\text{m}}$).

Graphite elements debonding results to be a common damaging mechanism characterized by a morphology that depends on microstructure. Relationships between voids morphology parameters are shown in Figs. 16 and 17.

Almost all the investigated voids are characterized by "$L > D$", for all the investigated microstructures. It implies that a ductile component in the debonding mechanism is always present. However, microstructure strongly affects the experimental results distribution. Pearlitic ductile iron is characterized by the lowest differences "$L - D$" (completely fragile debonding corresponds to "$L - D = 0$"), and fully ferritic ductile iron is characterized by the higher "$L - D$" values (higher ductile deformation during debonding). Ferritic–pearlitic ductile iron shows intermediate "$L - D$" values distribution. This is probably due to the different mechanical behaviour of ferritic shields and pearlitic matrix that induces a compression stress state in ferritic shields corresponding to K_{min}, with a consequent increase of the importance of plasticity induced crack closure effect and a decrease of the crack growth rate. Graphite spheroids ductile debonding appears to be reduced, if compared to ferritic ductile iron (lower "$L - D$" values). Austempered ductile iron is characterized by "$L - D$" experimental results distribution that is similar to ferritic–pearlitic ductile iron and probably crack closure mechanisms are the same as in ferritic–pearlitic ductile iron, due to the presence of residual ferrite around graphite elements. Also voids depths "M" analysis as a function of the approximation sphere diameters "D" suggests to obtain an analogous classification of the importance of the ductile deformation in the debonding mechanism, with the fully pearlitic microstructure that is characterized by "$M \leqslant D/2$" (completely fragile spheroids debonding) and other investigated microstructures that are characterized by a higher impor-

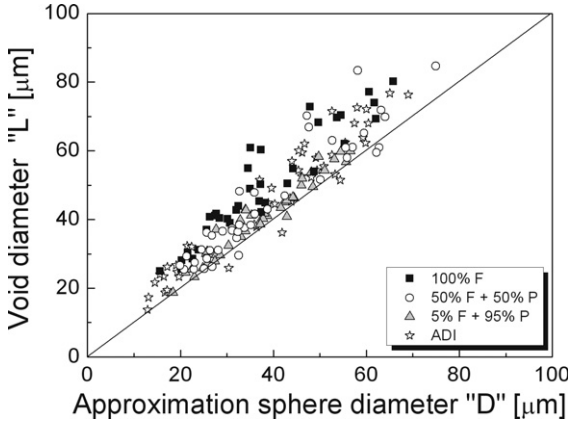

Fig. 16. Approximation sphere diameter–void diameter as a function of microstructure.

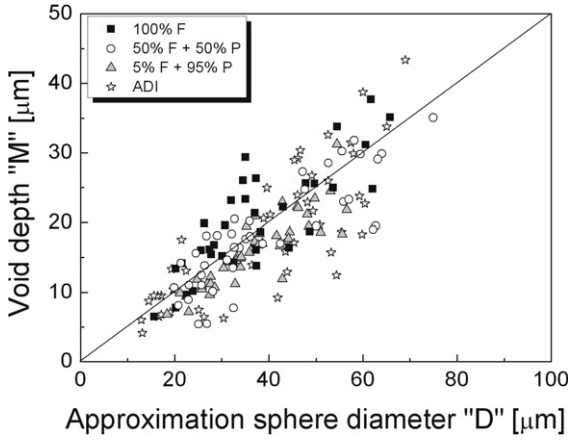

Fig. 17. Approximation sphere diameter–void depth as a function of microstructure.

tance of the ductile deformation in the debonding mechanism, with a consequent higher scatter of the experimental results.

Metal matrix microstructure influence on graphite spheroids debonding micromechanisms and its influence on crack tip stress distribution is summarized in Fig. 18. Considering fully ferritic or fully pearlitic ductile irons, graphite elements debonding is an important crack closure mechanism: higher ductile deformation corresponds to lower crack growth rates. Ferritic–pearlitic or bainitic–ferritic microstrucutre are characterized by a similar phases distribution with a pearlitic or bainitic matrix and ferritic shields around graphite elements (more evident in ferritic–pearlitic ductile iron). Considering that both pearlite and bainite are characterized by a reduced ductility and higher UTS values, if compared to ferrite, it is possible to propose a second peculiar closure effect due to the different mechanical behaviour of ferritic shields and of pearlitic or bainitic matrix. During the loading cycle, the ferrite and pearlite (or bainite) deformation level could be really different, especially corresponding to higher R and ΔK values:

- corresponding to K_{max} values, ferritic shields are more deformed than pearlitic (or bainitic) matrix;
- corresponding to K_{min} values, pearlitic (or bainitic) matrix induces on ferritic shields a residual compression stress condition with a consequent enhancing of the closure effect.

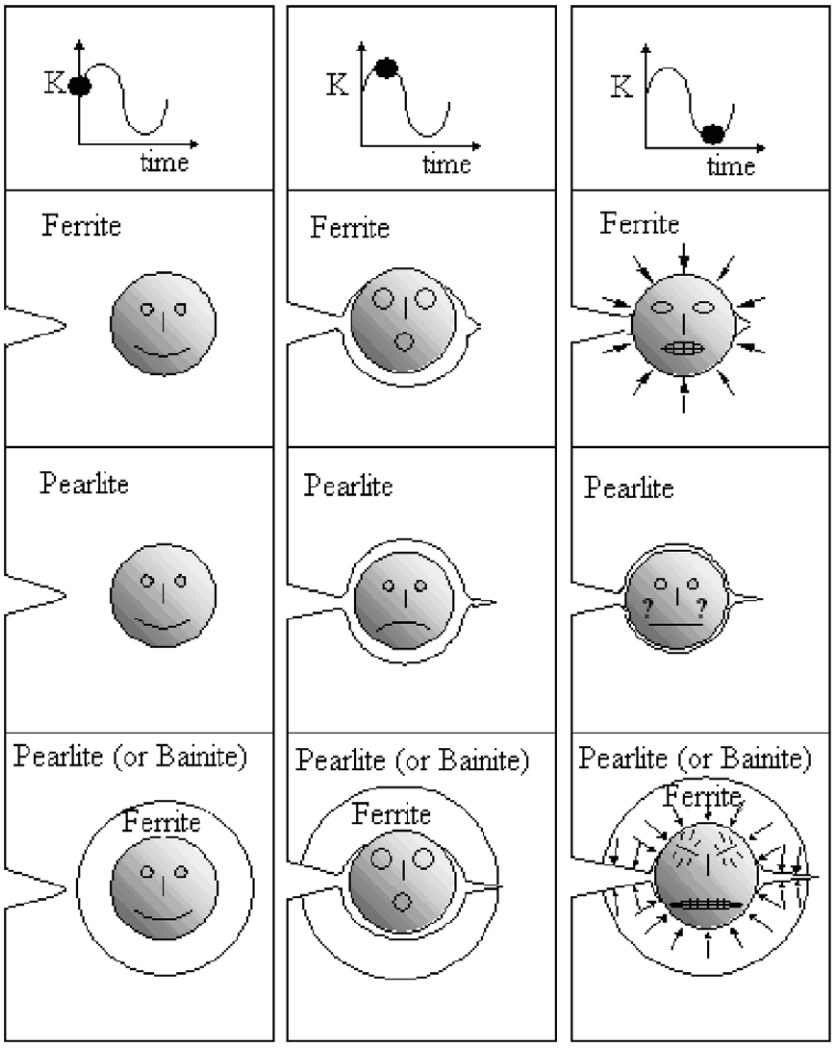

Fig. 18. Ductile and fragile graphite elements debonding influence on crack closure effect in ductile irons.

Considering both the fatigue crack propagation tests results and the fatigue crack propagation micromechanisms investigation, it is possible to outline that the higher fatigue crack propagation resistance of the ferritic–pearlitic and of austempered ductile irons depends on crack closure mechanisms. Higher R and ΔK values enhance matrix microstructure and spheroids influence. For these loading conditions:

- graphite spheroids ductile debonding in ferritic and ferritic–pearlitic (or bainitic) ductile iron implies a "spheroid presence induced" crack closure effect and
- different mechanical behaviour of ferrite and pearlite (or bainite), and the peculiar phases distribution in ferritic–pearlitic or ferritic–bainitic ductile irons, imply an increase of the importance of the crack tip plasticity induced crack closure effect that mainly acts on ferritic shields.

4. Conclusions

In this work, microstructure influence on ductile iron fatigue crack propagation resistance was investigated considering three ferritic–pearlitic ductile irons and an austempered ductile iron. Fracture surface was investigated by means of light optical microscope crack profile analysis and by means of SEM fracture surface analysis. A quantitative analysis of 3D reconstructed surfaces was performed, mainly focusing the graphite nodules debonding mechanisms.

Experimental results allow to summarize the following considerations:

- Microstructure influences ductile irons fatigue crack propagation resistance only considering high R values; at lower R values, similar crack growth rates are obtained.
- SEM fracture surface analysis allowed to quantify the importance of graphite elements ductile debonding as a crack closure mechanism for ferritic or pearlitic ductile irons.
- Fully ferritic and fully pearlitic ductile irons fatigue crack propagation resistance is affected by the ductile graphite elements debonding: higher ducitle debonding level corresponds to lower fatigue crack growth rate values.
- Ferritic–pearlitic and austempered ductile irons are characterized by a peculiar phases distribution (ferritic shields around graphite elements embedded in a pearlitic or bainitic matrix) and this implies the activation of a second crack closure mechanism an increase of the importance of a crack tip plasticity induced crack closure effect due to the different mechanical behaviour of ferrite and pearlite (or bainite) and to the peculiar phases distribution.

References

[1] Ward RG. An introduction to the physical chemistry of iron and steel making. London: Arnold; 1962.
[2] Labrecque C, Gagne M. Ductile iron: fifty years of continuous development. Can Metall Quart 1998;37(5):343–78.
[3] ASTM standard test method for measurements of fatigue crack growth rates (E647-93). Annual Book of ASTM Standards. 0301, American Society for Testing and Materials; 1993.
[4] Iacoviello F, Di Cocco V. Fatigue crack paths in ferritic–pearlitic ductile cast irons In: International conference on fatigue crack paths, Parma, Italy; 2003. p. 116.
[5] Tokaji K, Ogawa T, Shamoto K. Fatigue crack propagation in spheroidal-graphite cast irons with different microstructure. Fatigue 1994;16:344–50.
[6] Iacoviello F, Di Bartolomeo O. Cavallini M. Resistenza alla propagazione delle cricche di fatica nelle ghise sferoidali austemperate In: AIM national conference, Vicenza, Italy; 2004. p. 19.
[7] Iacoviello F, Cavallini M. Influenza della microstruttura sulla propagazione di cricche di fatica nelle ghise sferoidali. La Metall Ital 2003:31–7.